Journal of Marine Research, 52, 25–53, 1994

Lateral entrainment in baroclinic currents

by Melvin E. Stern[1] and Jean-Raymond Bidlot[1]

ABSTRACT

A two layer shear flow model with piecewise uniform potential vorticity is used to show that circulation or free exchange of parcels in an isopycnal layer of uniform potential vorticity can be greatly inhibited by a strong potential vorticity front in another isopycnal layer. On the other hand, a net mass transfer across the edge of a shear flow can be produced by the initial presence of a strong mesoscale eddy. The entrainment resulting from this eddy-shear flow interaction is defined and quantified for an ensemble of initial realizations. It is suggested that dynamically similar entrainment processes, occurring in more realistic potential vorticity distributions, are important in coupling the recirculation gyres to the Gulf Stream, thereby providing the observed downstream increase in transport.

1. Introduction and statement of the problem

Beyond the Straits of Florida the transport of the Gulf Stream increases with downstream distance at a rate much greater than can be accounted for by the wind-driven Sverdrup gyre, and the required influx is supplied by mean recirculation gyres on either side of the stream [Knauss (1969), Richardson *et al.* (1969), Hogg *et al.* (1986)]. The increase occurs whether one measures the stream using long time Eulerian averages, or ensembles of synoptic "streamwise coordinates" [Halkin and Rossby (1985)]. In the latter case, which is more pertinent to our subsequent work, the downstream direction is defined in terms of the synoptic axis of the stream, which is constructed (essentially) by drawing that curve on the ocean's surface connecting points whose vector velocity has maximal amplitude relative to those on a vertical section normal to the velocity. Of particular concern to our discussion of entrainment is the "edge" of the stream, which is conventionally defined by the points on the normal section where the downstream velocity vanishes. A counterflow (negative or zero downstream velocity) exists outside the edge curve, and thus the outside parcels must have their velocity reversed in the (synoptic) time interval in which they cross the meandering edge. The integrated downstream velocity within the edges of a given section defines the local transport, whose observed downstream increase must be supplied by the spatially integrated horizontal velocity (v_n) directed normal to (and

1. Florida State University, Department of Oceanography B-169, Tallahassee, Florida, 32306-3048, U.S.A.

relative to) the meandering edge. A similar property must occur for the time averaged relative velocity $\bar{v}_n$ of the streamwise realizations. Figure 6b of Halkin and Rossby (1985) is one realization of a synoptic section, with a fully resolved inshore edge, which is noteworthy because it has vanishingly small normal velocity v_n. Their Figure 10c, on the other hand, shows that the time averaged $\bar{v}_n$ at the inshore edge is directed inward toward the axis, with a value of 6 cm/sec in the thermocline and 3 cm/sec below. The difference between the synoptic v_n and the mean $\bar{v}_n$ indicates significant eddy fluctuations at the edge of the stream, as also appears in other observations [Lee and Waddell (1983), Bower and Rossby (1989)]. The relatively large value of the eddy fluctuations suggests that they may be dynamically important in coupling the stream to the ambient region, which must ultimately supply the fluid for the increasing stream transport. The time averaged mass transport requirement in streamwise coordinates might be satisfied by a mean gyre whose streamlines lie partially inside and partially outside the edge. But the value of v_n at the edge of any isopycnal layer must be sufficiently large to allow circulating gyre parcels to overcome potential vorticity constraints along their path. The nature of these constraints and the way in which they can be overcome will be considered.

In Sections 2–4 a two layer quasi-geostrophic model is used (Fig. 1), with H_1 denoting the mean thickness of the upper layer, H_2 the mean thickness of the lower layer, g^* the reduced gravity, and f the uniform Coriolis parameter. The undisturbed mean flow has piecewise uniform potential vorticity, with velocity $\bar{u}^*(y') = 0$ on one side of the undisturbed interface ($y' = 0$), and $\bar{u}^*(y') = -s\lambda_0 \sinh(y'/\lambda_0)$ at $y' \leq 0$, where $s = -\partial\bar{u}^*(0^-)/\partial y'$ and $\lambda_0 = (g^*H_1)^{1/2}/f$. The undisturbed lower layer velocity is assumed to vanish, and thus the downward deflection h^* of the interface is geostrophically given by $\bar{u}^*(y') = -(g^*/f)\partial\bar{h}^*(y')/\partial y'$.

The question of the potential vorticity constraint on the circulation of a weak velocity field is addressed in Figure 1, where this field is produced by a point *barotropic* vortex with strength Γ^* placed at a fixed distance point $y' = R^* \gg \lambda$. This artifice (having no similarity to real ocean recirculation gyres) merely serves to force a weak transverse velocity in both layers at the edge ($y' = 0$) of the baroclinic shear flow. It is apparent that the resulting deflection L' (Fig. 1) of the potential vorticity front will prevent the Γ^* circulation from entering into the upper shear layer [see the linear theory for the 1½ layer model of Stern and Flierl (1987)]. But if the potential vorticity gradient vanishes in the lower layer, then it might be supposed [Bower *et al.* (1985)] that there would be little opposition at $y' = 0$ to the Γ^* circulation, in which case it would result in a greatly increased value of the maximum vertically integrated transport under the jet. This supposition is incorrect, however, because the thermal wind equation requires that any transverse lower layer velocities must produce potential vorticity anomalies (see Eqs. 2.2) in the overlying frontal layer, and these will in turn induce new transverse velocities in the lower layer which opposes the forced gyre velocities (Sec. 3). The quantitative extent of this effect will be illustrated

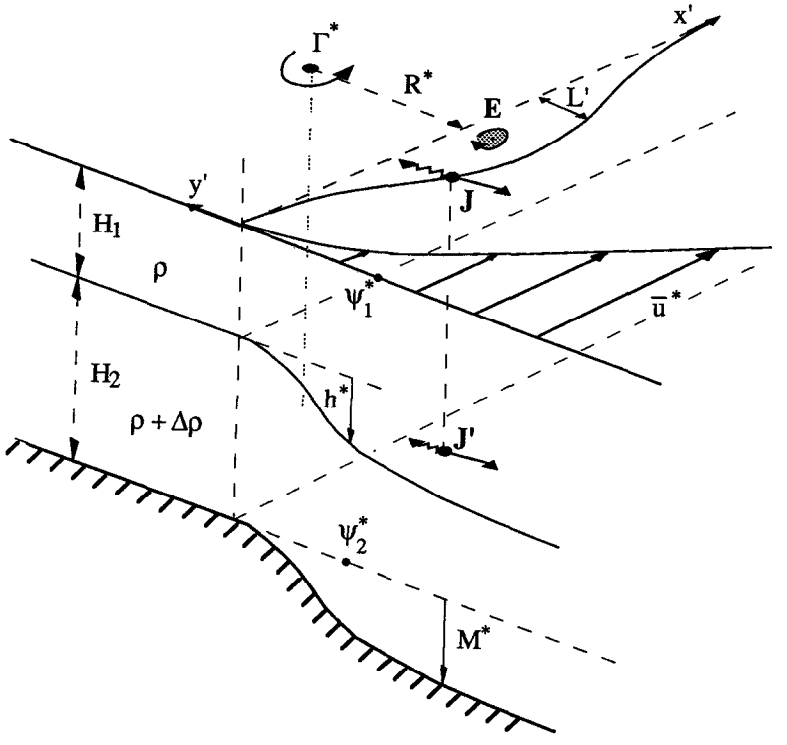

Figure 1. Perspective diagram of a two layer model with an undisturbed shear flow $\bar{u}^*(y')$ in the light upper layer, and with piecewise uniform potential vorticity. A fixed point barotropic vortex of strength Γ^* at $y' = R^*$ deflects the potential vorticity interface to $y' = L'$ (steady state solution). The downward deflection of the density interface is h^*, and ψ_1^*, ψ_2^* are the respective values of the dynamic pressure in the upper and lower layers. The bottom topography M^* is chosen (see text) so that the lower layer is resting with everywhere uniform potential vorticity in the undisturbed state. E is a typical anticyclonic potential vorticity anomaly associated with L', and it induces transverse upper and lower layer velocities as indicated by the wiggly arrows at J and J'. These oppose the velocities (straight arrows) induced by Γ^*.

by choosing a bottom topography $M^*(y') = \bar{h}^*(y')$, so that the lower layer with vanishing undisturbed velocity also has completely uniform potential vorticity. A less "artificial" choice of a flat bottom ($M^*(y') = 0$) would produce a finite gradient of potential vorticity in the lower layer, further inhibiting the transverse velocity, and merely emphasizing the point made by the simpler model (Sec. 3), viz. transverse velocities in any isopycnal layer depend on isopycnal potential vorticity gradients in all layers.

The remainder of the paper shows how the constraints on weak mean motion normal to mean potential vorticity contours may be overcome by the presence of strong mesoscale fluctuations of potential vorticity (eddies) close to the stream's

edge. The subsequent eddy-shear flow interaction may produce an entrainment similar (in a restricted sense) to that which occurs in the turbulent flow of a jet from a nozzle (or smokestack), where the eddies draw irrotational ambient fluid into the shear flow, thereby increasing its transport downstream. But the similarity ends here, since the oceanic eddies are generated quite differently. They may, moreover, pre-exist in the ocean gyres and be slowly advected toward the jet's edge, at which stage the relatively rapid process of incorporating the eddy [Bane *et al.* (1989)] and its surrounding fluid begins.

The entrainment mechanism is isolated in Sec. 4 by removing the gyre of Sec. 3 from the relatively rapid eddy-shear flow interaction (cf. Fig. 2a). A similar kind of barotropic interaction leading to entrainment was calculated by Stern (1991).

Stern and Flierl (1987) considered the strong interaction of a point baroclinic vortex located close to the edge of a shear flow in a "1½ layer" model, but those calculations did not extend long enough in time for entrainment to be computed. Some of the qualitative effects in the Stern and Flierl model appeared in a primitive equation model [Smith and Davis (1989)] with continuous potential vorticity for the shear flow and the eddy. But the greatly increased degrees of freedom allowed the appearance of other kinds of eddy-shear flow interaction, and it is noteworthy that the eddy entrainment effect appeared in only one of Smith and Davis' many runs. This suggests the importance of exploring many simple special models to identify all entrainment favorable potential vorticity configurations.

Two such models are studied herein, for the purpose of illustrating the mechanism of entrainment, defining it, and computing it for an ensemble of single eddy-shear flow realizations. In the first model (Fig. 2a), an eddy with potential vorticity P_e is strongly interacting with the non-inflected shear flow $\overline{u}(y)$ as used in the previous section. The second (Fig. 2b) model consists of a full jet with different potential vorticities on each side of its axis. Stern and Flierl (1987) also made limited time calculations for this case, and showed that an anticyclonic (cyclonic) *point* vortex originally on the cyclonic (anticyclonic) shear side of the jet is eventually drawn toward and across the axis, an effect similar to the one observed [Bane *et al.* (1989)] for a cyclone on the seaward side of the Gulf Stream. The present calculations extend those of Stern and Flierl (1987) by computing total entrainment volumes, not only for point potential vortices of various strengths and initial positions but also for an eddy of finite area. The main results [Eqs. (4.5), (4.7), (5.6), and Fig. 11] may be useful in designing and interpreting two layer (and other) entrainment models, where the number of relevant non-dimensional numbers becomes even larger than in our case. Although our models shed light on the eddy entrainment mechanism, they cannot be applied directly to an actual eddy and the actual Gulf Stream because the qualitative nature of the interaction depends on the detailed distribution of potential vorticity in all isopycnal layers. But in the conclusions (Sec. 6 and Fig. 12) we suggest how the ideas developed may be qualitatively extrapolated to more realistic potential vorticity distributions.

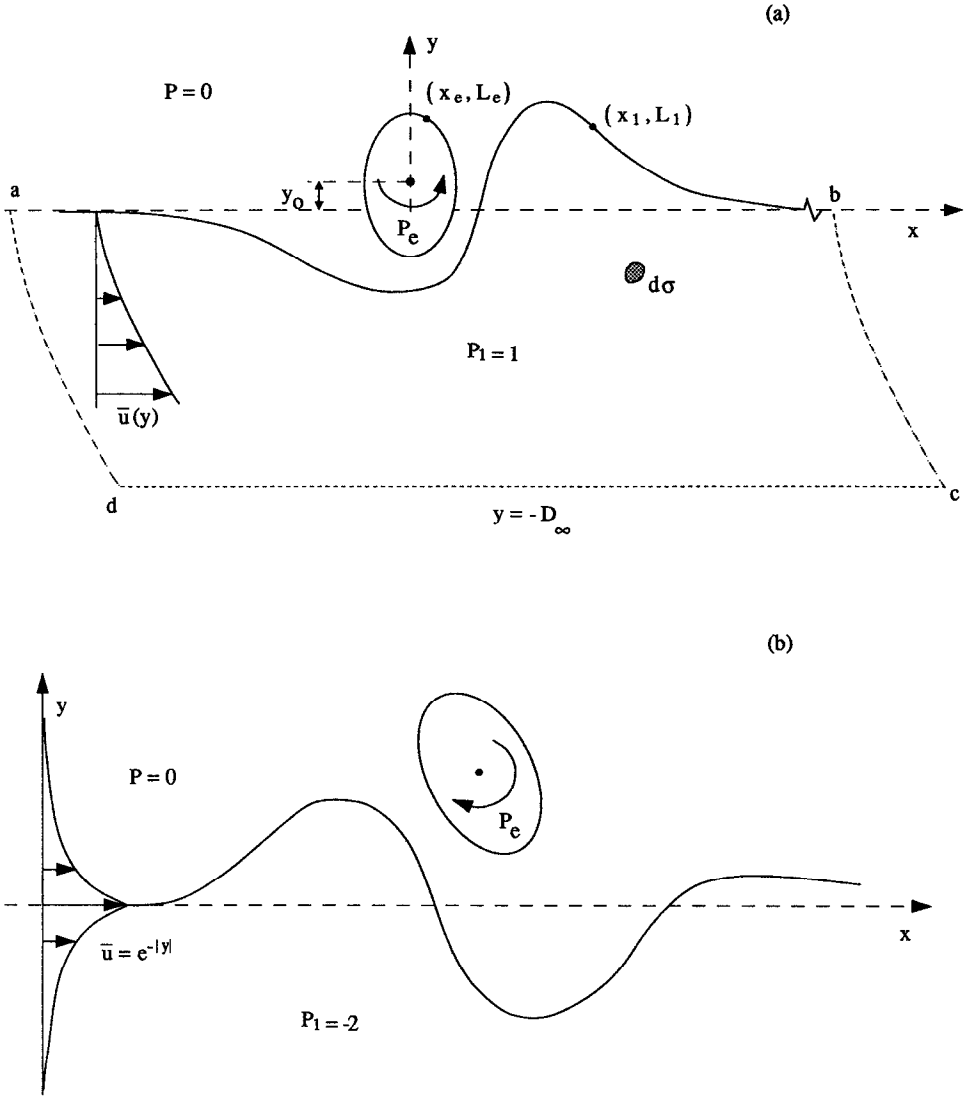

Figure 2. The onset of entrainment in the 1½ layer model ($H_2 = \infty$). (a) A finite cyclonic eddy of uniform potential vorticity $P = P_e$ interacts with the edge of $y = L_1(x_1, t)$ of a shear layer which has $P = P_1$ for $y < L_1$ and $P = 0$ for $y > L_1$. The boundary of the eddy is given by $y = L_e$, and its centroid is at $y = y_0(t), x = 0$ in the moving coordinate system. See Appendix B for the usage of the closed material curve abcd. (b) Same as (a) except that the interaction of a full jet with an anti-cyclonic eddy ($P_e < 0$) is considered.

2. Two isopycnal layers with $M^*(y') = \bar{h}^*(y')$

The two conserved quasi-geostrophic potential vorticities are $\omega_1^* = \nabla^2\psi_1^*/f^2 - h^*/H_1$ and $\omega_2^* = \nabla^2\psi_2^*/f^2 + [h^* - M^*(y')]/H_2$, where the top ($\psi_1^*$) and bottom ($\psi_2^*$) dynamic pressures are related by the hydrostatic equation $\nabla\psi_1^*(x', y', t') = \nabla\psi_2^* +$

$g^* \nabla h^*$. Let $\{\psi'_1, \psi'_2, h', \omega'_1, \omega'_2\}$ denote the departure of the total fields from the respective undisturbed fields $\{\psi^*_1(y'), \overline{\psi}^*_2, \overline{h}^*_1, \overline{\omega}_1, 0\}$, and subtract the contribution of the latter from the potential vorticity equations. Since $\overline{h}^*(y') = M^*(y')$ we get

$$\nabla^2\psi'_1/f^2 - h'/H_1 = \omega'_1, \tag{2.1a}$$

$$\nabla^2\psi'_2/f^2 + h'/H_2 = \omega'_2, \tag{2.1b}$$

$$\psi'_1 = g^*h' + \psi'_2. \tag{2.1c}$$

The potential vorticity "anomaly" ω'_1 vanishes at $y = \infty$, and has two components, one of which is due to the eddy in the upper layer. The other component, due to the deflection $L'(x', t')$ of the upper layer interface, equals the actual potential vorticity minus the undisturbed $\overline{\omega}^*_1(y')$. For example, if $0 < y' < L'(x', t')$ where L' is the ordinate of the disturbed potential vorticity interface (Fig. 1), then $\omega'_1(x', y', t') = (s/f) - 0$, whereas $\omega'_1 = 0 - (s/f)$ if $0 > y' > L'$. The interpretive utility of the "anomalies" is due to the fact that they account for all the y' velocity (whereas $\overline{u}^*(y')$ must be added in to obtain the total x'-velocity). The velocities are then evaluated on the interfaces of all the piecewise uniform domains, thereby obtaining the Lagrangian components (eg. dx'/dt', dL'/dt') for all interfacial points, and from which the temporal evolution of the shear flow and eddies is obtained using the well known contour dynamical method. The technique used here is a combination of that used by Stern and Flierl (1987) and Stern (1991). Neither the methods nor models used below are novel, but the focus is entirely on obtaining an understanding and quantification of baroclinic entrainment in the simplest cases. See Meacham (1991) for a more elaborate technique applied to the baroclinic instability problem.

By subtracting (2.1a, 2.1b) an equation for h' is obtained, and by addition an equation for the barotropic pressure $H_1\psi'_1 + H_2\psi'_2$ is obtained. When these are non-dimensionalized using $\lambda = (g^*/f^2)^{1/2}(1/H_1 + 1/H_2)^{-1/2}$ as the length scale, s^{-1} as the time scale, $s\lambda$ as the velocity scale and $\psi' = fs\lambda^2\psi, h' = (fs\lambda_2/g^*)h, L' = \lambda L_1, \omega'_1 = (s/f)\omega_1, \omega'_2 = (s/f)\omega_2$, the result is

$$\nabla^2 h - h = \omega_1 - \omega_2, \tag{2.2a}$$

$$\nabla^2(\epsilon\psi_1 + \psi_2) = \epsilon\omega_1 + \omega_2, \tag{2.2b}$$

$$\psi_1 = h + \psi_2, \tag{2.2c}$$

$$\epsilon = H_1/H_2. \tag{2.3}$$

The upper layer velocity (u_1, v_1) and lower layer velocity (u_2, v_2) are then obtained from

$$v_1 = \partial\psi_1/\partial x, \qquad v_2 = \partial\psi_2/\partial x, \qquad u_2 = -\partial\psi_2/\partial y, \tag{2.4a}$$

$$u_1 = \frac{-\partial\psi_1}{\partial y} - \frac{1}{\mu}\begin{cases} 0 & y > 0 \\ \sinh y\mu & y < 0 \end{cases}, \qquad \mu = \lambda/\lambda_0 = (1+\epsilon)^{-1/2} \tag{2.4b}$$

As previously mentioned, ω_1 has two components, one of which is due to the anomalies created by the L_1-displacements, and the other (denoted by subscript "e") is due to the eddy, i.e.

$$\omega_1 = (\omega_1)_e + \begin{cases} 1 & 0 < y < L_1 \\ -1 & 0 \geq y \geq L_1 \\ 0 & \text{otherwise} \end{cases}, \tag{2.5a}$$

whereas ω_2 has only one component

$$\omega_2 = (\omega_2)_e, \tag{2.5b}$$

which is due to the eddy.

The barotropic Green's function to be used in solving (2.2b) is logarithmic, whereas the baroclinic Green's function for (2.2a) is Bessel's K_0. From the combination of these Green's functions and (2.2c) the important fact emerges that an element of potential vorticity at any point (x, y) in either layer induces circulations (clockwise or counterclockwise) whose sense is the *same* in both layers.

3. Weak eddy-shear flow interaction

Our first task, as indicated in Sec. 1, is to illustrate the inhibition of bottom layer influx by an upper layer potential vorticity gradient (Fig. 1), employing the simple flow forced by a distant point barotropic vortex at $y = R = R^*/\lambda$ with equal non-dimensional strengths

$$\Gamma = \iint (\omega_1)_e \, dx\, dy = \iint (\omega_2)_e \, dx\, dy, \tag{3.1}$$

in both layers. The total y-velocity depends on two components, one of which $v_\Gamma(x, y)$ is induced by (3.1), and this velocity at $y = 0$, or

$$v_\Gamma(x, 0) = \frac{\Gamma}{2\pi} \frac{x}{R^2 + x^2} \tag{3.2}$$

will force some steady interfacial displacement $y = L_1(x)$. The potential vorticity anomalies associated with L_1 induce another component of y-velocity, denoted by $v_1(x, y)$, $v_2(x, y)$ in the top and bottom layers, respectively. Since $\bar{u}(0) = 0$ the interfacial *equilibrium* condition for small perturbations ($R \gg 1$ or $\Gamma \ll 1$) is

$$-v_1(x, 0) = v_\Gamma(x, 0). \tag{3.3}$$

As shown in Appendix A, the solution of this equation is considerably simplified by

introducing the half-range ($k > 0$) Fourier transforms

$$\begin{pmatrix} v_\Gamma(x,0) \\ L_1(x) \\ v_1(x,y) \\ v_2(x,y) \end{pmatrix} = Re \begin{pmatrix} -i\Gamma/2\pi \int_0^\infty dk\, e^{-(R-ix)k} \\ \int_0^\infty dk\, e^{ikx} \hat{L}(k) \\ \int_0^\infty dk\, e^{ikx} \hat{v}_1(k,y) \\ \int_0^\infty dk\, e^{ikx} \hat{v}_2(k,y) \end{pmatrix} \tag{3.4}$$

in which case $\hat{v}_1(k,y)$ and $\hat{L}(k)$ are related by algebraic equations, and for $y = 0$ the formal relation is

$$i\Omega(k)\hat{L}(k) = -\hat{v}_1(k,0). \tag{3.5}$$

(The coefficient of proportionality Ω has an independent physical significance, viz. it equals the frequency of free ($\Gamma = 0$) interfacial sinusoidal waves.) The value of Ω computed (in Appendix A) from Eqs. (2.2) with linearized matching conditions across the $y = 0$ discontinuity is

$$\Omega = \frac{1}{2(1+\epsilon)} \left[\frac{k}{(1+k^2)^{1/2}} + \epsilon \right]. \tag{3.6}$$

By using (3.4), (3.5) and (3.6) we then get

$$\hat{L}(k) = \frac{\Gamma e^{-kR}}{2\pi\Omega(k)}, \tag{3.7}$$

$$L_1(x) = -\frac{\Gamma}{\pi}(1+\epsilon)\, Re \int_0^\infty dk \frac{e^{-k(R-ix)}}{\epsilon + k(1+k^2)^{-1/2}}. \tag{3.8}$$

In the interesting limit $R \to \infty$, $\epsilon = 0(1)$, a transformation of variables (k, x, y) to $(kR, x/R, y/R)$ shows that it is permissible to set $k = 0$ in the denominator of (3.8) which then simplifies to

$$L_1(x) = -\frac{\Gamma(1+\epsilon)}{\pi\epsilon} \frac{R}{R^2 + x^2} \qquad (R \to \infty). \tag{3.9}$$

The normal mode calculation (Appendix A) also gives $\hat{v}_1(k,y)$, $\hat{v}_2(k,y)$ as exponential functions of y, and the quantity of greatest interest $v_2(x,y)$ is then obtained from (3.4). For the $R \to \infty$ limit (mentioned above) the asymptotic velocity is

$$v_2(x,y) = \frac{\Gamma}{2\pi} Re \int_0^\infty dk\, ie^{-k(R+|y|-ix)} = -\frac{\Gamma}{2\pi} \frac{x}{(R+|y|)^2 + x^2}, \tag{3.10}$$

and for $y < 0$ this becomes

$$v_2(x, y) = -\frac{\Gamma}{2\pi} \frac{x}{(R - y)^2 + x^2} = -v_\Gamma(x, y). \tag{3.11}$$

This important result means that the net y-velocity $v_2(x, y) + v_\Gamma(x, y)$ vanishes under the shear layer ($y < 0$), to the leading order in the $1/R$ expansion. The significance of this can be appreciated by noting that if $v_\Gamma(x, y)$ were unopposed (or even fractionally opposed) in the lower layer it would add an infinite value to the vertically integrated transport under the shear layer, since the integral of $v_\Gamma(x, 0)$ from $x = -\infty$ to $x = 0$ diverges. But the actual velocity $v_\Gamma(x, 0) + v_2(x, 0)$, and the actual transport in the bottom layer are much smaller because of the compensation induced by the anomalies in the upper layer with the strong potential vorticity variation.

A qualitative explanation of the effect can be obtained from Figure 1, where the solid arrows at points (J, J') represent the y-velocity due to Γ^*. For a steady state front the velocity at J produced by the shear flow anomalies (as indicated by the wiggly arrow at J) must be equal and opposite. The sense of the wiggly arrows clearly requires L' to have anti-cyclonic anomalies; i.e., $L' < 0$. The typical anti-cyclonic element "E" induces anti-cyclonic circulation in the lower layer, as well as the upper layer, and the wiggly arrow at J' indicates the resultant velocity induced by all the upper layer anomalies. Thus the induced velocity in the lower layer also opposes (to some extent) the velocity induced by Γ^*.

To obtain the quantitative measures of the extent of the opposition to the lower circulation we must go to the next order in the $1/R$ expansion to find the small finite value of the total transverse velocity beneath the surface front. As computed in Appendix A the value is

$$v_2(x, 0) + v_\Gamma(x, 0) = \frac{\Gamma}{\pi} \frac{(1 + \epsilon)}{\epsilon} \frac{xR}{(x^2 + R^2)^2} \qquad R \to \infty, \qquad \epsilon = 0(1), \tag{3.12}$$

and this is indeed smaller than the forcing velocity (3.2) by $0(1/R)$. The plausible generalization is that a weak barotropic velocity (v_Γ) will induce potential vorticity anomalies at a strong upper layer front, which can oppose the (original) lower layer velocity, and prevent most of it from crossing under the frontal edge. The isopycnal potential vorticity gradient in any layer of a shear flow affects the normal velocity in all other layers.

How might the presence of a strong eddy near the edge of the jet gyre boundary overcome this constraint and enable a weak mean exterior circulation (a gyre) to be incorporated under the jet? This will eventually require a consideration of the two layer problem, beginning with the simplest one in Eqs. (2.2)–(2.4).

4. Entrainment in the 1½ layer model

But it is necessary, as mentioned in Sec. 1, to first extend previous calculations of the nonlinear interaction between the shear flow (Fig. 1) and an upper layer eddy when $\epsilon = 0$, $\psi_2 = 0 = \omega_2$ in (2.2)–(2.4). Figure 2a is a schematic diagram of this 1½ layer model, and Figure 2b is for the case of a full jet interacting with an eddy.

The interface $y = L_1(x_1, t)$ in Figure 2a separates the shear flow of potential vorticity $P = P_1 = 1$ from the ambient fluid of potential vorticity $P = 0$, whereas $y = L_e(x_e, t)$ bounds the eddy of potential vorticity $P = P_e = (\omega_1)_e$ and strength

$$\Gamma = \iint P_e \, dx \, dy. \tag{4.1}$$

(In Section 4b the initial state (see Fig. 5b) is such that part of the L_e, L_1 interfaces are in contact with each other.)

Eqs. (2.2a) is an inhomogenous Bessel equation for h, from which the total upper layer velocity

$$v(x, y, t) = \partial h / \partial x, \tag{4.2a}$$

$$u(x, y, t) = -\partial h / \partial y + \bar{u}(y), \tag{4.2b}$$

is computed. The contribution (v_e, u_e) from the eddy is given by the clockwise integral

$$\begin{pmatrix} v_e \\ u_e \end{pmatrix} = -\frac{P_e}{2\pi} \oint \begin{pmatrix} dL_e \\ d\xi_e \end{pmatrix} K_0((x - \xi_e)^2 + (y - L_e(\xi_e))^2)^{1/2} \tag{4.3}$$

and the contribution from the shear flow is

$$v_1 = -\frac{1}{2\pi} \int_{\xi_1=-\infty}^{\xi_1=\infty} dL_1 K_0((x - \xi_1)^2 + (y - L_1(\xi_1))^2)^{1/2}, \tag{4.4a}$$

$$u_1 = \bar{u}(y) - \frac{1}{2\pi} \int_{\xi_1=-\infty}^{\xi_1=\infty} d\xi_1 \{K_0((x - \xi_1)^2 + (y - L_1(\xi_1))^2)^{1/2} - K_0((x - \xi_1)^2 + y^2)^{1/2}\}, \tag{4.4b}$$

where K_0 is the Bessel function. As previously mentioned, evolutionary equations for L_1, L_e are obtained by evaluating $(v_e + v_1, u_e + u_1 + \bar{u})$ on the contours and setting it equal to the appropriate $(dL/dt, dx/dt)$. These integral equations are then reduced to a large number of ordinary differential equations by introducing discrete Lagrangian points along the contour, by approximating the integrals using the trapezoidal rule, and by marching in time with a second order Runge-Kutta approximation. The (approximate) boundary condition is zero velocity at the (finite) endpoints. Lagrangian points are inserted or deleted as necessary to maintain interior resolution on the stretching contours. To maintain sufficiently small values of L_1 in the neighborhood of its ends, additional points at large $|x|$ were added as necessary, and some of these open boundary condition runs (see Tables 1 and 2) were checked by using periodic

Table 1. Evolution of a point potential vortex of strength $\Gamma = 1$, initially at $y_0(0) = .6$, with a cyclonic shear layer initially at $L_1(x, 0) = 0$. c is the downstream velocity of the vortex, and the integral of L_1 is over all x, Q is a theoretical invariant, and dM/dt is the spatially integrated momentum flux in the $+y$ direction. An equivalent calculation using periodic (wavelength = 20) boundary conditions was also performed for this case, and it yielded $y_0 = .374, c \times 10^2 = 7.29$ at $t = 26$.

t	$y_0(t)$	$c \times 10^2$	$\int L_1\, dx$	Q	M
0	.6		0	.6	.180
2	.575	1.52	3.7×10^{-4}	.6001	.165
4	.525	3.99	2.3×10^{-4}	.5999	.137
6	.482	5.44	1.1×10^{-3}	.5994	.114
8	.452	6.07	8.0×10^{-4}	.5992	.099
10	.431	6.45	6.3×10^{-4}	.5989	.088
12	.415	6.75	9.0×10^{-4}	.5986	.082
14	.403	6.98	3.7×10^{-4}	.5985	.077
16	.395	7.06	8.0×10^{-4}	.5993	.074
18	.391	7.03	1.3×10^{-4}	.5995	.071
20	.389	6.97	1.7×10^{-4}	.5993	.069
22	.387	6.95	1.03×10^{-3}	.5993	.066
24	.384	6.95	4.49×10^{-3}	.5990	.064
26	.379	7.09	4.50×10^{-3}	.5982	.062

conditions in x. See Stern (1985, 1991) for related procedural details, and related checks.

If $L_1 = 0$ at $t = 0$, a cyclonic eddy (Fig. 2a) will obviously induce $v > 0$ at $x > 0$ and $v < 0$ at $x < 0$, thereby producing at $t > 0$ an interface L_1 with positive potential vorticity anomalies under the ridge ($L_1 > 0$), and negative anomalies above the trough. It is intuitively clear that the resultant of all of these anomalies yields $v < 0$ at the centroid $x_0(t), y_0(t)$ of the eddy, thereby moving it closer to $y = 0$. This increases the displacement of the L_1 ridge, and causes it to wind counterclockwise around the eddy. Eventually the winding ridge filament may come into "close contact" with the L_1-*trough* [i.e. the upstream ($L_1 < 0$) branch of the interface], thereby irreversibly embedding both the eddy and its surrounding $P = 0$ fluid inside a "new" interface of the shear flow, as described below, and as occurs in the purely barotropic case [Stern (1991)]. The main difference between the two cases is that the baroclinic Green's function K_0 has a much shorter range of influence than the barotropic Green's function, and this should be borne in mind in future consideration of the full two layer problem, in which the long range barotropic Green's function will appear.

a. Results for a point vortex close to a shear layer. Consider first the simpler version of Figure 2a which occurs for a cyclonic point vortex $\Gamma > 0$ located initially at some small $y_0(0) > 0$, and $L_1(x, 0) = 0$. Then (4.3) is replaced by a velocity field $\Gamma/2\pi\, dK_0(r)/dr$ directed perpendicular to the line of length r connecting the vortex to any

Table 2. dM/dt is the spatially integrated momentum flux and Q is the numerical value of the quadratic invariant for a point potential vortex at $y_0(t)$. The time dependence is listed for three values of the vortex strength Γ, and the total entrained area at the end of each run is also given. An equivalent calculation using periodic (wavelength = 20) boundary conditions was performed for $\Gamma = 1$, and at $t = 18$ it yielded $y_0 = -.298$ with the entrained area equal to .967.

	$\Gamma = 1$			$\Gamma = .5$			$\Gamma = .25$		
t	$y_0(t)$	M/Γ	Q/Γ	y_0	M/Γ	Q/Γ	y_0	M/Γ	Q/Γ
0	.200	0	.200	.200	0	.200	.200	0	.200
2	.081	−.014	.198	.117	−0.12	.196	.153	−.008	.200
4	−.035	−.025	.199	−.001	−.024	.195	.065	−.024	.199
6	−.123	−.032	.198	−.076	−.033	.201	−.002	−.027	.199
8	−.178	−.038	.199	−.113	−.039	.208	−.040	−.033	.201
10	−.202	−.042	.201	−.146	−.042	.204	−.063	−.037	.201
12	−.235	−.043	.199	−.192	−.043	.195	−.086	−.039	.200
14	−.263	−.044	.195	−.233	−.045	.191	−.105	−.040	.193
16	−.272	−.043	.190	−.247	−.046	.187	−.112	−.040	.189
18	−.306	−.043	.184	−.253	−.046	.181	−.116	−.041	.190
	Entrained Area = .97			Entrained Area = .58			Entrained Area = .37		

(x, y). In all the following calculations the $x = 0$ origin is fixed relative to the center of the moving vortex, and c denotes its absolute speed. [Special precautions are necessary in evaluating the last Bessel integral in (4.4b) when the vortex crosses the $y = 0$ axis because of the (integrable) singularity.]

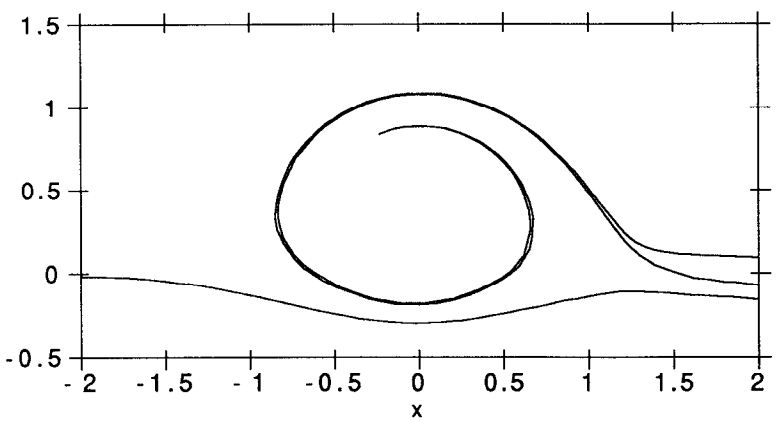

Figure 3. Moderate nonlinear interaction of a point vortex initially at $y_0(0) = .6$, $\Gamma = 1$, with a shear layer interface at $L_1(x, 0) = 0$. The figure (for $t = 26$) shows that the trough of the L_1 interface is directly under the point vortex ($x_0(0) = 0$, $y_0 = .38$). In addition, there is a "tearing" effect in which a thin filament from the edge of the shear layer is captured by the vortex and wound around it.

Figure 3 and Table 1 for $y_0(0) = 0.6$ and $\Gamma = 1$ illustrate a transitional regime between linear (Sec. 3) and strong interactions. As previously mentioned the initial tendency is for an L_1 ridge (trough) to be induced downstream (upstream) of the vortex, thereby accounting (Table 1) for the negative values of $v = dy_0/dt$ at early times. The subsequent reduction in $|dy_0/dt|$, and increase in absolute vortex speed c, is due to the greater downstream phase propagation of the L_1-*trough*, until its center phase locks at $x = 0$ under the point vortex (Fig. 3). The quantity Q in Table 1 is an integral invariant (derived in Appendix B) whose small numerical variation provides a check on the reliability of the calculation. Another check on the numerics can be obtained from the integrated L_1 in Table 1, which indicates the extent of the compensation of the areas bounded by the trough (Fig. 3) and the ridge in the finite x-interval of integration (which is only partially shown). The time derivative of the quantity M in Table 1 (Appendix B) is the spatially integrated momentum flux, which is counter-gradient in this case. The qualitative difference between this moderate interaction and the weak interaction of linear theory is the "tearing" of the interface (Fig. 3), such that a very thin filament from the edge of the shear layer is captured by the vortex and wound counterclockwise around it.

A well known computational problem, requiring contour surgery arises when the two branches of a filamentary winding (Fig. 3) come too close relative to the time step of the integration. The numerical problem is compounded when $y_0(0)$ is reduced (Fig. 4) because many more thin windings develop, and adjacent windings also come closer as time increases. It was therefore necessary to limit the number of windings as well as the thickness of each one. For present purposes the compromise arrived at in obtaining Figure 4 was to delete the tip point (of the first and innermost winding) when the distance between its two neighboring points was $\frac{1}{5}$ of the average distance between Lagrangian points. Although the surgery leads to a systematic error in the area bounded by L_1, this error was small compared to the value of the entrained area computed below.

The stronger interaction in Figure 4 is characterized by a rapid capture of the vortex by the shear layer, and by a relatively thick outer winding of $P = 1$ fluid (the unstippled region). Note that this branch of L_1, coming from $x = +\infty$ and winding counterclockwise, is approaching (as $t \to \infty$) a contact (at $-1.8 < x < 0$) with the L_1 branch coming from $x = -\infty$. For all intents and purposes a multiply connected L_1-curve is about to form, as appears explicitly if a (vertical) "cut" of the two branches is made at (say) $x_c \approx -1.8$ (where $\partial L_1(x_c)/\partial x = \infty$), and then joining vertically adjacent ends. The result consists of a "new" singly connected shear flow interface going continuously from $x = -\infty$ to x_c to $x = +\infty$, inside of which the remaining portion of the L_1 curve surrounds ambient $P = 0$ (stippled) fluid. The entrained area is defined as the total amount of this fluid which is transported across the new potential vorticity surface. The value of this area appears in the last row of Table 2, and the uncertainty due to the "cutting" is less than or equal to the absolute error ($\sim 2 \times 10^{-2}$) in the integrated L_1. The aforementioned tip surgery appears to

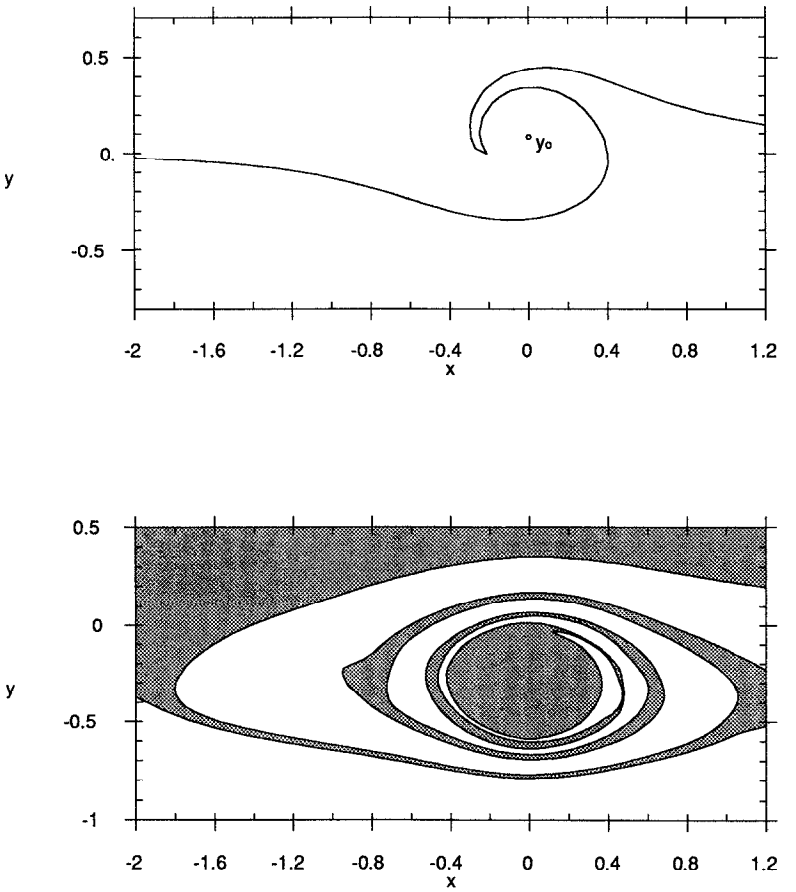

Figure 4. A strong interaction when $y_0(0) = .2, L_1(x, 0) = 0, \Gamma = 1$. (a) At $t = 2$ (top), $y_0 = .081$. (b) At $t = 18$ (bottom), the upstream branch of L_1 has wound counterclockwise around the point vortex ($y_0 = -.31$) and is about to make "contact" with the upstream branch. The stippled area designates ambient ($P = 0$) fluid, part of which is about to be entrained inside the "new" interface (see text) of the shear flow (see Table 2).

be the source of the increasing error in Q (Table 2) at $t > 14$, since no "significant" change occurred when the Runge-Kutta time step was halved. For smaller Γ (Table 2), similar effects are found with smaller entrained area, smaller vortex penetration, and smaller countergradient momentum flux.

Some calculations using Eqs. (4.3)–(4.4) were also made (not shown) for a round eddy (Fig. 2) separated by a finite distance from the shear flow, but the windings in this case presented an even more severe numerical problem because they come close to the finite eddy perimeter as well as to themselves. Nevertheless, no qualitative difference from the point vortex regime appeared, and therefore we now turn to an initial condition which is a limiting case of Figure 2a, having a lesser degree of

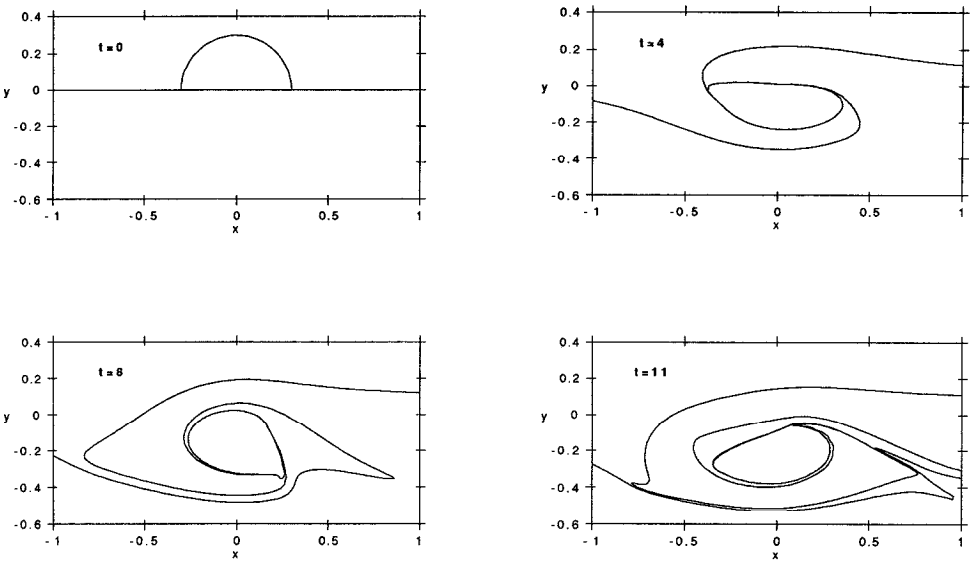

Figure 5. A semi-circular cyclonic eddy of radius 0.3, potential vorticity $P_e = 2.5$, and circulation $\Gamma = .353$ is initially in close contact with the cyclonic shear flow interface $L_1(x, 0) = 0$. At $t = 11$ the round eddy and its surrounding $P = 0$ fluid are entrained inside the "new" interface found by cutting L_1 at $x \sim -.75$. See Table 3, row 5.

filamentary windings and consequently requiring no tip surgery in any of the calculations which follow.

b. A round eddy in close contact with a shear flow. Figure 5a shows a semi-circular patch of potential vorticity P_e, part of whose perimeter L_e is in contact with $L_1(x, 0)$. Although a circle or ellipse is the simplest representation of an eddy not in contact with a front, a semi-circle or semi-ellipse is a reasonable representation of a patch of high potential vorticity at the edge of a shear flow, resulting from its prior advection by the ambient gyre (as previously mentioned). For this case the integrations in Eqs. (4.3–4.4) require special consideration for the points on the contact segment, such that their velocity is computed only once. The evolution (Fig. 5) is qualitatively similar to that of a point vortex (Table 2, Fig. 4) with nearly the same Γ. In Figure 5 the centroid decreases from $y_0(0) = .127$ to $y_0(10) = -.196$ (see Table 3) and the spatially averaged momentum flux (not shown) was again found to be counter-gradient ($dM/dt < 0$). The invariance of Q was maintained to 3% at $t = 11$, at which time the right hand branch of L_1 (Fig. 5) has wound counter-clockwise around the eddy, making virtual contact at $x = -.75$ with the left hand branch. The new interface formed by "cutting" at this point gives a total entrained area ($A = .32$) which is essentially the same whether the (subjective) cut is made at $t = 9$, 10, or 11. Note that A consists of the entire P_e eddy in addition to the surrounding $P = 0$ fluid.

Table 3. Summary of total entrained area A in shear layer for vorticies of different circulation (Γ), semi-major axis (b), semi-minor axis (a), and potential vorticity P_e. t_e is the time at which A is computed, and $\bar{y}(t)$ is the ordinate of the centroid of the vortex.

Γ	a	b	$y_0(0)$	P_e	A	t_e	$y_0(t_e)$	A/Γ
.25	0	0	.2	$-\infty$	.37	18	−.12	1.48
.5	0	0	.2	∞	.58	18	−.25	1.16
1.	0	0	.2	∞	.97	18	−.30	.97
.21	.3	.3	.13	1.5	.24	14	−.22	1.15
.35	.3	.3	.13	2.5	.32	11	−.23	.91
.49	.3	.3	.13	3.5	.38	11	−.32	.77
.49	.42	.42	.18	1.75	.53	15	−.17	1.07
.35	.6	.15	.06	2.5	.32	15	−.33	.91
.35	.6	−.15	−.06	2.5	.38	14	−.46	1.09
1.18	1.	1.	.42	.75	2.25	28	−.18	1.91
1.57	1.	1.	.42	1.	2.34	26	−.12	1.49
1.96	1.	1.	.42	1.25	2.54	24	+.03	1.29
2.75	1.	1.	.42	1.75	2.88	20	−.05	1.05

The same A = .32 was obtained when only the shape of the initial eddy was changed to a semi-ellipse with downstream semi-axis a = .6 and cross-stream semi-axis b = +.15. Figure 6 shows what happens when the sign of b is reversed, (i.e., the elliptical eddy was placed below the $L_1 = 0$ interface), and Table 3 shows that the total entrained area is only slightly changed. [The momentum flux (not shown in Table 3) is down-gradient ($dM/dt > 0$) in this case, suggesting that the time

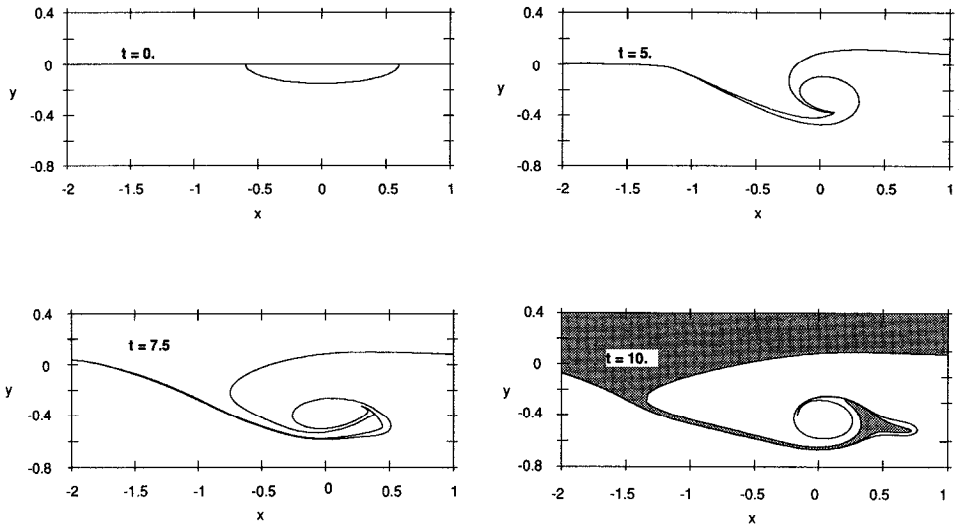

Figure 6. Same as Figure 5 except that the eddy is elliptical and initially located inside the shear flow (a = .6, b = −.15). The stippled region is part of the ambient P = 0 fluid. The entrained area (see Table 3) was computed at t = 14 (not shown).

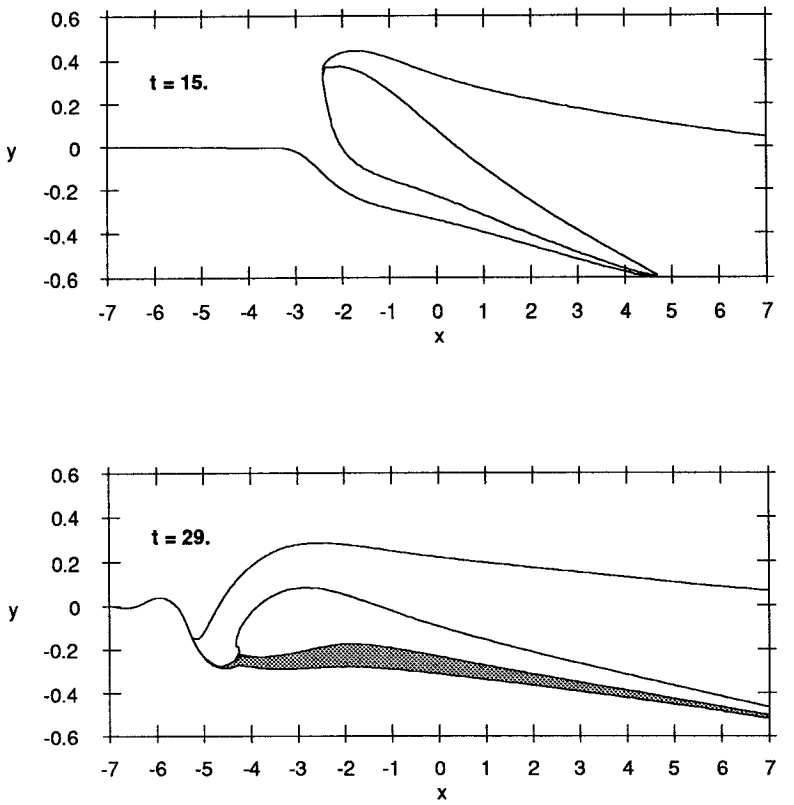

Figure 7. Same as Figure 5 except $P_e = .75$, $a = 1$, $b = 1$. Entrainment occurs even through $P_e < P_1$.

integrated momentum flux is counter-gradient only for eddies initially outside the shear flow.]

Entrainment can also occur for an eddy with potential vorticity somewhat smaller than the shear flow, provided it is initially in close contact. Figure 7 shows the result for an initially semi-circular eddy with $a = b = 1$ and $P_e = .75$. The centroid decreases from $y_0(0) = .42$ to $y_0(26) = -.17$, and the total entrained area at $t = 24$ was only .5% smaller than at $t = 29$.

Table 3 lists all the calculations made for shear flow entrainment, including the point vorticities ($P_e = \infty$), and the main generalization for the total entrained area A is given by

$$\alpha = \frac{A}{\Gamma} = 1.3 \pm 0.6. \tag{4.5}$$

The physical significance of α becomes clear when (4.5) is converted to dimensional units (denoted by primes). Since $P_e = (s/f)^{-1}(\nabla^2\psi'_e - h'_e/H_1)$, and since the inte-

grated relative vorticity ($\nabla^2\psi'_e$) of an eddy vanishes, the conversion of Γ is

$$\Gamma = \iint P_e \, dx \, dy = f / (\lambda_0^2 s) \iint (-h'_e/H_1) \, dx' \, dy'. \tag{4.6}$$

By substituting this and $A = A'/\lambda_0^2$ we find that the dimensional value of the entrained volume is

$$A'H_1 = \frac{\alpha}{\Delta P'} \iint (-h'_e) \, dx' \, dy'. \tag{4.7}$$

where

$$\Delta P' = s/f, \tag{4.8}$$

is the change in potential vorticity across the shear layer interface. Eq. (4.5) then implies the "constant" α equals the volumetric entrainment ($A'H_1$) multiplied by $\Delta P'$ and divided by the (temporally invariant) integral of the isopycnal anomaly ($-h'_e$).

5. Interaction of a vortex with a full jet

To isolate the interaction of a vortex with the potential vorticity gradient near the axis ($y' = 0$) of a full jet we consider an undisturbed velocity profile $\bar{u}^*(y') = s\lambda_0 \exp -|y'|\lambda_0^{-1}$ with vanishing geostrophic potential vorticity for $y' > 0$, and uniform potential vorticity

$$P_1^* = -2s/f \tag{5.1}$$

for $y' < 0$, where s denotes the largest shear and λ_0 the radius of deformation. This is again used as the length unit, and s^{-1} is the time unit, so that the non-dimensional current becomes

$$\bar{u}(y) = e^{-|y|} \tag{5.2}$$

and the potential vorticity at $y < 0$ becomes

$$P_1 = -2. \tag{5.3}$$

This multiplicative factor must be introduced in Eqs. (2.5) and (4.4) for the case (Fig. 2b) of a jet whose potential vorticity interface $L_1(x, t)$ is disturbed by an eddy of potential vorticity P_e and strength Γ. Aside from the minor modifications due to the new end-conditions $v(\pm\infty, t) = 0$, $u(\pm\infty, t) = 1$ on L_1, the calculation proceeds as in the previous section. Although the results below are given for an anticyclonic vortex ($\Gamma < 0$) whose centroid is located initially at $y_0(0) > 0$, mirror symmetry exists for the case of a cyclone placed on the anti-cyclonic shear side of the jet (see Fig. 12b).

It is easy to see (Fig. 2b) that if $L_1(x, 0) = 0$, then an anti-cyclone $\Gamma < 0$, at $y_0(0) > 0$ will initially induce a ridge ($L_1 < 0$) with negative anomalies at $x < 0$ and a trough with positive anomalies at $x > 0$, and these anomalies will then cause the anti-cyclone

to move to smaller y or larger $\bar{u}$. Thus the amplitude of L_1 increases more as the vortex approaches the jet axis, and the advective speed (c) of the vortex also increases. Furthermore, the translating vortex forces a relatively long free "lee wave" on the jet's axis [see linear theory of Stern and Flierl (1987)], and the temporally increasing wave energy requires compensating decrease in $y_0(t)$ [see the Q-invariant in Appendix B]. The combination of all of these effects causes a much stronger interaction in this case (e.g. Fig. 2b) than in the shear layer case (e.g. Fig. 2a).

a. Point vortex interacting with the jet. This stronger interaction can be seen in Figure 8 since the initial value of $y_0(0) = 1.5$ is much larger than in Figure 3, and yet the point vortex has moved toward $y = 0$, and has crossed the interface at the time shown (note the lee wave at $x > 0$). The enlarged view (Fig. 8) shows the area (stippled) of the $P = 0$ fluid entrained inside the $P = -2$ fluid and across the new potential vorticity interface, which goes from $x = -\infty$ to the "cut" point ($x = 2$) and then to $x = +\infty$. The time variation of the parameters is indicated in Table 4 for another run having an even larger $y_0(0)$. No winding surgery was used in any of these calculations, and the error in the Q invariant is only 1%. Note that the momentum flux dM/dt (Eq. B.8) is relatively large and positive for the jet (compared to the shear layer). Figure 8 and Table 4 are typical of the results obtained for all of the five runs in Figure 9, which shows the variation in entrained area as Γ and $y_0(0)$ are changed. The plotted points are acceptably close to the straight line

$$A = \tfrac{2}{3}(-\Gamma) \tag{5.4}$$

and the deviations may be partially due to a small parametric dependence on $y_0(0)$.

It is interesting to compare the jet entrainment (5.4) with the shear layer entrainment (4.7), taking into account that the potential vorticity change across the jet interface

$$\Delta P' = \frac{2s}{f} \tag{5.5}$$

is twice as large as (4.8). Substitution of $A = A'/\lambda^2$ and (4.6) into (5.4) then yields the volumetric entrainment

$$A'H_1 = \frac{2}{\Delta P'}\left(\frac{2}{3}\right)\int\int h_e' \, dx' \, dy'. \tag{5.6}$$

This is the same as (4.7, 4.5), for all intents and purposes, thereby achieving a significant "collapse" of a rather extensive parametric space.

b. Round eddy interacting with a full jet. Now consider an initially circular eddy with radius R_0, centroid $y_0(0) > 0$, and uniform potential vorticity $P_e < 0$. The contour

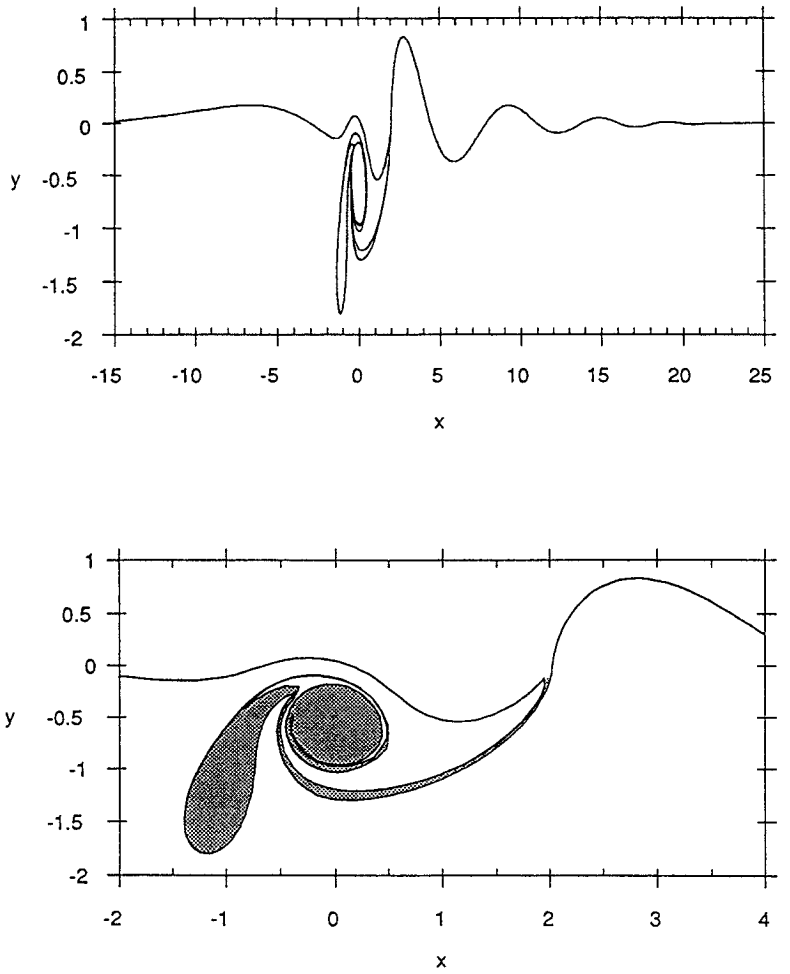

Figure 8. Entrainment of a point vortex by a full jet having piecewise uniform potential vorticity. At $t = 0$ the interface (the jet axis) is on $y = 0$, $\Gamma = -2$, $y_0(0) = +1.5$. The upper diagram shows the position of the interface at $t = 33.5$, and the lower diagram is a close up view of the entrainment. The vortex is at $y_0(33.5) = -.58$, and the entrained stippled fluid also originated at $y > 0$. A "cut" is made at $x \approx 2$ on the jet axis to form the new potential vorticity interface. A completely analogous (mirror symmetry) process occurs for a cyclone $\Gamma = +2$ located initially at $y_0 = -1.5$, in which case fluid from $y < 0$ is entrained across the jet interface and into the cyclonic shear region.

dynamical equations are the same as Eqs. (4.2)–(4.4b), except for the fact that (4.4a, b) must be multiplied by -2 [the change in potential vorticity across the undisturbed jet (5.2)]. The winding problem in this case was not severe and no surgery was required, unlike the previously mentioned case of a shear layer interacting with a round eddy.

Table 4. The interaction of a full jet $\bar{u}(y) = \exp -|y|$ with a point vortex of strength $\Gamma = -4$ at $y_0(0) = 2$. $c(t)$ is its speed, q is the quadratic invariant, and dM/dt is the integrated momentum flux.

t	$y_0(t)$	$c(t)$	$Q(t)$	$M(t)$
0	2		−.8000	0
4	1.99	.14	−.8000	+.10
8	1.96	.14	−.8000	.76
12	1.90	.15	−.8000	.78
16	1.82	.17	−.8001	1.4
20	1.71	.18	−.8002	2.2
24	1.55	.21	−.8004	3.4
28	1.29	.24	−.8006	5.1
32	.80	.29	−.799	7.7
34	.35	.23	−.799	9.2
36	−.13	.19	−.799	10.5
38	−.50	.19	−.800	11.5
40	−.75	.22	−.800	12.1
42	−.94	.20	−.803	12.2
44.5	−1.05	.21	−.810	12.0

Entrained area = 2.62

If $0 > P_e > -2$ the eddy is drawn toward the axis of the jet (Fig. 10) and partially coalesces with the current on the same side of the deformed interface. On the other hand if $P_e < -2$ (Fig. 11) the eddy and some of its surrounding fluid ($P = 0$) cross to the opposite side of the jet axis. By "cutting" at the close contact point ($x \approx 3$), the

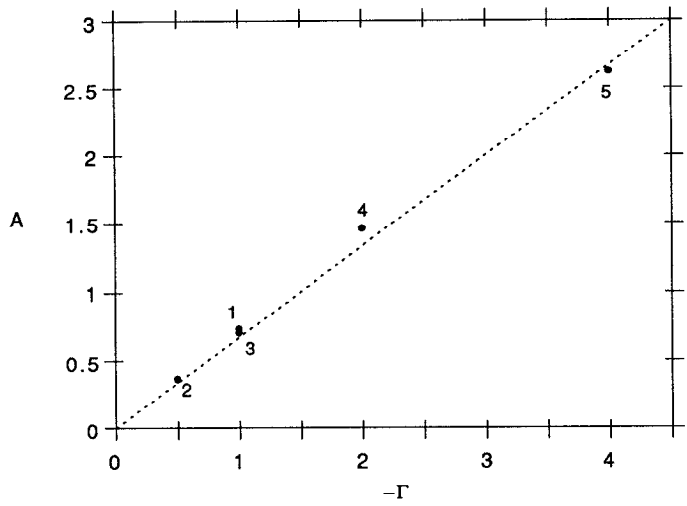

Figure 9. Non-dimensional area *(A)* entrained in a full jet for various Γ, $y_0(0)$. The time at which the entrainment is computed is t_e and the data for the numbered points are: (1) $t_e = 23, y_0(0) = 1$, (2) $t_e = 39, y_0(0) = 1$, (3) $t_e = 54, y_0(0) = 1.5$, (4) $t_e = 33.5, y_0(0) = 1.5$, (5) $t_e = 44.5, y_0(0) = 2$.

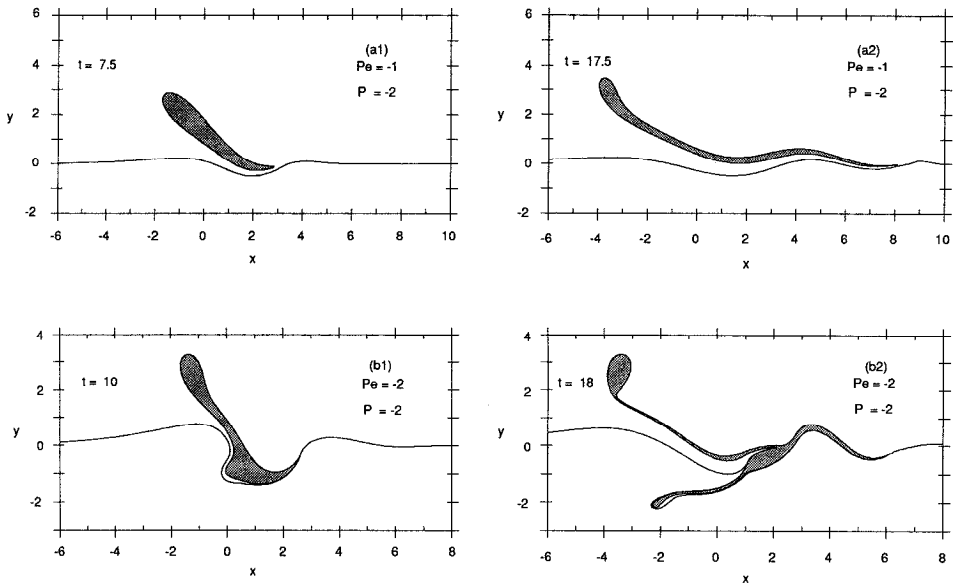

Figure 10. Interaction of a round eddy with a full jet. A circular anti-cyclone of unit radius and uniform potential vorticity $P_e < 0$ is initially located at $y_0(0) = +1.5$ on the cyclonic side of an undisturbed ($L_1(x, 0) = 0$) jet $\bar{u} = \exp - |y|$. (a1 and a2) the stippled eddy with $P_e = -1$ is drawn toward the jet axis. The $x = 0$ origin of the coordinate system moves downstream with the centroid $[y_0(17.5) = +1.22]$. (b1 and b2) same as above except $P_e = -2$ and y_0 (18) = .52. Part of the eddy is captured and comes into close contact with the jet axis but very little entrainment across the potential vorticity interface occurs.

total entrained area was found to be

$$A = 4.2. \tag{5.7}$$

This is somewhat larger than the eddy area (π), and somewhat smaller than the value of (5.4) for a point vortex having the same strength ($-\Gamma = 3\pi$). The coalescence

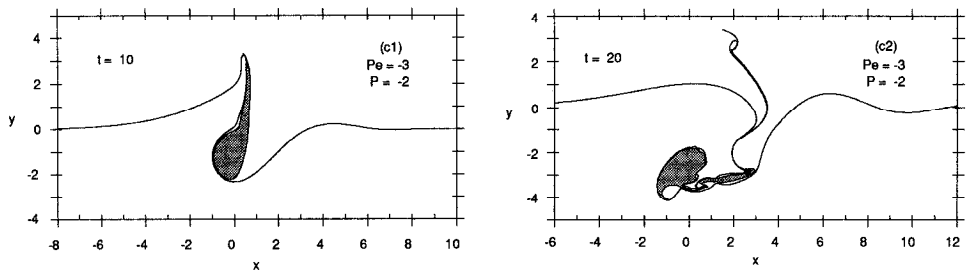

Figure 11. Same initial conditions as Figure 10 except $P_e = -3$, and now $y_0(20) = -2.8$. By cutting the interface at the close contact point ($x = 3$) a new jet interface is formed, across which a net mass flux has occurred. Note the small blob at $y \approx 2.8$ containing anticyclonic ($P = -2$) fluid from the jet, which has also been transported across the new interface.

effect in Figure 10 appears to be similar to the capture of a small barotropic eddy by another one with much larger area [cf. Fig. 1a in Melander *et al.* (1987)].

6. Conclusions and suggestions

The general idea has been advanced (supported by the example in Sec. 3) that a strong isopycnal potential vorticity gradient in the upper layer of a jet not only prevents weak transverse motions from entering that layer, but also greatly inhibits the entrance of ambient fluid into the lower layer, even if that layer has vanishing potential vorticity gradient. This suggests that effective incorporation of a large-scale mean gyre incident on a strong jet requires the (intermittent) presence of strong potential vorticity fluctuations (mesoscale eddies) at the gyre-jet boundary.

Two relatively simple baroclinic shear flow models were used to illustrate the mechanism by which an exterior eddy and its surrounding fluid are "entrained," this being defined as the net volume transfer across mean potential vorticity surfaces of the jet. An ensemble of such calculations have been made for an eddy initially located near the edge of a shear layer, and also for an eddy near the axis of a full jet. This initial state is supposed to have been brought about by the prior (slow) gyre advection of anomalies toward the jet. The main results [Eqs. 4.5, 4.7, 5.6] achieve a partial collapse of the entrainment, in the ensemble of our 1½ layer model calculations. The entrainment calculations need to be extended to the full two layer case.

The inhibiting effect on the lower layer circulation (Fig. 1) was discussed for the case in which upper layer velocity, vorticity, and potential vorticity increase in the same sense. Does the same effect occur if the potential vorticity (P) decreases (Fig. 12a) as the other two quantities increase, which occurs in the undisturbed state when the variation in upper layer thickness dominates the relative vorticity term. Figure 12a also shows the small perturbations in the $P < 0$ isolines (dashed) induced by a distant cyclonic barotropic point vortex Γ^*, and v_Γ^* (solid arrows) denotes its contribution to the y-velocity on the interface (bold face curve). At greater y, $P \equiv 0$, and at lesser y, $P < 0$. On the $P = 0$ interface the total horizontal velocity is infinitesimal (since $\bar{u}^*(0) = 0$), and if a steady state (Fig. 12a) exists then v_Γ must be balanced by the resultant (wiggly arrow) anomalies associated with all the deflected potential vorticity lines. The sense of these wiggly arrows requires anti-cyclonic P anomalies, which in turn require displacement of the P-isolines as shown (note that these deflections are opposite to the interface deflection in Fig. 1). Moreover, as in Figure 1, those upper layer anti-cyclonic anomalies produce a lower layer velocity in the same sense as the wiggly arrows, and therefore, they still oppose the lower layer v_Γ^*. This supports the generalization of one of our two main results.

Figure 12b suggests how the strong eddy-jet interaction computed in Figures 10 and 11 might be generalized to the case of a continuous variation of potential vorticity (the dashed lines). This distribution has some resemblance to the structure across the Gulf Stream at 29N [Leaman *et al.* (1989)], where the potential vorticity

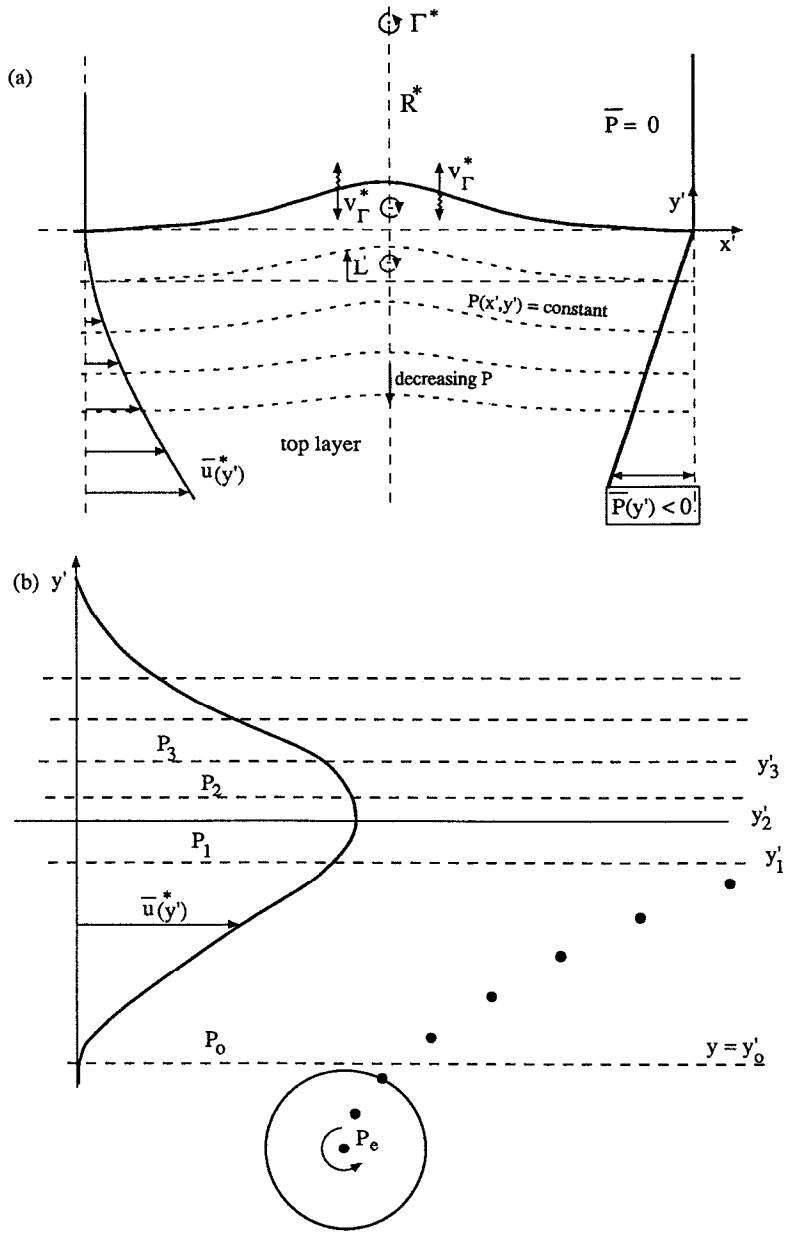

Figure 12. (a) A generalization of Figure 1 when the undisturbed potential vorticity ($\overline{P}$) of the upper layer is increasing with y' (for $y' < 0$), and the corresponding shear flow $\overline{u}^*$ is decreasing to $\overline{u}^*(0) = 0$. Above the interfacial curve (the solid line) the potential vorticity and its derivative are identically zero. In the steady state the constant potential vorticity lines (dashed curves) are deflected an infinitesimal distance $L'(x', y')$ by a distant ($R^* \gg \lambda$) barotropic point vortex (Γ^*). (b) This figure shows the initial condition of an undisturbed jet $\overline{u}^*(y')$ in a 1½ layer model with potential vorticity increasing monotonically with $y'(P_0 < P_1 < P_2 < P_3)$, but with a potential vorticity gradient in $y'_1 > y' > y'_0$ which is weak compared to the gradient on the cyclonic side of the jet. Also shown is the initial state of a cyclonic eddy with potential vorticity $P_e \approx P_1$. The conjectured subsequent movement of the centroid of the eddy due to its interaction with the jet is schematically indicated by dark dots. See text.

gradient is weak on the anti-cyclonic side of the jet in the thermocline. In Figure 12b P_0 is the potential vorticity at the edge ($\bar{u}(y'_0) = 0$) of the undisturbed jet, and the gradient of potential vorticity is positive (i.e., $P_0 < P_2 < P_3$), with a very small gradient between y'_1 and y'_0. At $t = 0$ (Fig. 12b) a cyclonic eddy of potential vorticity $P_e \approx P_1$ is assumed outside the edge, and at $t > 0$ the counterclockwise circulation induced by this deflects P_1, P_2, P_3 in such a sense that their associated anomalies cause the centroid of the eddy to move on a path indicated by the heavy dots. This conjecture is supported by Figures 10 and 11, which have similar but reversed distributions (i.e., an anticyclonic is initially on the cyclonic side of the undisturbed jet in Sec. 5). The latter calculations (cf. Fig. 10) suggest that the $P_e \approx P_1$ eddy in Figure 12b should end up with its centroid near $y = y'_1$, and with the P_0 isopleth wound around it to form a new "edge" in which the eddy is entrained. If the event is repeated by having new cyclones successively advected to $y < y'_0$ by the weak velocity in an external gyre (not shown), then an average transport of gyre water across the jet's edge is implied.

Acknowledgments. Partial support by the Office of Naval Research and the National Science Foundation is gratefully acknowledged.

APPENDIX A

Normal Mode Calculations for Sec. 3

To derive the important results (3.11, 3.12) for the lower layer velocity $v_2(x, y)$ induced by $L_1(x)$ anomalies we have to compute the Fourier transforms $\hat{v}_2(k, y)$, $\hat{v}_1(k, y)$ associated with the free wave problem. Accordingly we set $[(\omega_1)_e = 0 = (\omega_2)_e]$ in Eqs. 2.2. and consider the normal mode problem, in which the *perturbation* potential vorticity vanishes on either side ($|y| > L_1$) of the disturbed interface. The modes obtained from (2.2a, b) are given by the exponential functions

$$ik\hat{h}(k, y) = \hat{v}_1(k, y) - \hat{v}_2(k, y) = (\hat{v}_1(k, 0) - \hat{v}_2(k, 0))e^{-|y|(1+k^2)^{1/2}}, \quad \text{(A.1a)}$$

$$\epsilon\hat{v}_1(k, y) + \hat{v}_2(k, y) = (\epsilon\hat{v}_1(k, 0) + \hat{v}_2(k, 0))e^{-k|y|}, \quad \text{(A.1b)}$$

where $\hat{h}(k, y)$ is the Fourier component of the interfacial height perturbation $h(x, y)$, and where the continuity of v from $y = 0^-$ to $y = 0^+$ has been used. The additional connection condition is most readily obtained by integrating 2.2a, b from $y = 0^-$ to $y = 0^+$, and by using the right-hand side of (2.5a) for ω_1. For either $L_1 > 0$ or $L_1 < 0$ the integration gives a discontinuity in the perturbation $\partial h/\partial y$ equal to L_1 and a discontinuity in $\partial/\partial y(\epsilon\psi_1 + \psi_2)$ equal to ϵL_1. Therefore the discontinuities in $\partial/\partial y$ $(\hat{v}_1 - \hat{v}_2)$ and $\partial/\partial y(\epsilon\hat{v}_1 + \hat{v}_2)$ are respectively equal to $ik\hat{L}$, $ik\epsilon\hat{L}$. When these two

relations are applied to (A.1a,b) the result is

$$-2(1 + k^2)^{1/2}(\hat{v}_1(k, 0) - \hat{v}_2(k, 0)) = ik\hat{L}, \tag{A.2a}$$

$$-2k(\epsilon\hat{v}_1(k, 0) + \hat{v}_2(k, 0)) = ik\epsilon\hat{L}, \tag{A.2b}$$

and therefore

$$\hat{v}_1(k, 0) = \frac{-i\hat{L}}{2(1 + \epsilon)}\left[\frac{k}{(1 + k^2)^{1/2}} + \epsilon\right], \tag{A.3}$$

$$\hat{v}_2(k, 0) = \frac{-i\epsilon\hat{L}}{2} + \frac{-i\hat{L}\epsilon}{2(1 + \epsilon)}\left[\frac{k}{(1 + k^2)^{1/2}} + \epsilon\right]. \tag{A.4}$$

At any y the velocity obtained from (A.1a,b) is

$$\hat{v}_2(k, y)\left(1 + \frac{1}{\epsilon}\right) = \left(\hat{v}_1(k, 0) + \frac{\hat{v}_2(k, 0)}{\epsilon}\right)e^{-k|y|} - (\hat{v}_1(k, 0) - \hat{v}_2(k, 0))e^{-(1+k^2)^{1/2}|y|}, \tag{A.5}$$

$$\hat{v}_1(k, y) = \hat{v}_2(k, y) + (\hat{v}_1(k, 0) - \hat{v}_2(k, 0))e^{-(1+k^2)^{1/2}|y|}. \tag{A.6}$$

The coefficient of proportionality in $\hat{v}_1(k, 0) = -i\Omega\hat{L}(k)$ obtained from (A.3) is

$$\Omega = \frac{1}{2(1 + \epsilon)}\left[\frac{k}{(1 + k^2)^{1/2}} + \epsilon\right], \tag{A.7}$$

as indicated in (3.6), and thereby verifying (3.8). The value of $v_2(x, y)$ is obtained by substituting (3.7) in (A.3) and (A.4), by using (A.5), and by using the last relation in (3.4). The leading term (3.11) in the $1/R$ expansion was shown to cancel the contribution of v_Γ at $y < 0$, and it only remains to show that (3.12) is the leading (non-vanishing) term for bottom layer velocity at $y = 0$. We first note that (A.1a) gives the total value of $\hat{h}(k, y)$ since the thermal wind equation implies that the barotropic v_Γ does not contribute (directly) to the difference in velocities in the two layers. Moreover, the *total* v at $y = 0$ in the upper layer must vanish in the *steady* state, and therefore the total transverse bottom layer velocity v at $y = 0$ is

$$v = -\frac{\partial h(x, 0)}{\partial x} \tag{A.8}$$

from Eqs. (A.1a) and (A.2a) we get

$$\hat{h}(k, 0) = \frac{-\hat{L}(k)}{2(1 + k^2)^{1/2}} = \frac{-\hat{L}(k)}{2}[1 + 0(k^2)], \tag{A.9}$$

and therefore the leading ($1/R \to 0$, or $k \to 0$, cf. 3.9) term for $h(x, 0)$ is

$$h(x, 0) = -\tfrac{1}{2}L(x). \tag{A.10}$$

It therefore follows from (A.8) and (3.9) that

$$v = \frac{-\Gamma(1+\epsilon)}{2\pi\epsilon}\frac{\partial}{\partial x}\frac{R}{R^2+x^2} \tag{A.11}$$

is the leading term for the *total* bottom layer velocity at $y = 0$, and this verifies (3.12).

APPENDIX B

The Q-invariant and the momentum flux

For a continuous distribution of potential vorticity $P(x, y, t)$ the quasi geostrophic flux is

$$\overline{vP} = \overline{v\left(\frac{\partial v}{\partial x} - \frac{\partial u}{\partial y} - h\right)} = -\frac{\partial}{\partial y}\overline{vu} \tag{B.1}$$

where the bar now denotes an integral over all x, and where (4.2ab) has been used. When (B.1) is multiplied by y and integrated from some $y = -D_\infty \to \infty$ (where $yv \to 0$) to $y = \infty$ the result is

$$\int_{-D_\infty}^{\infty} \overline{vu}\, dy = \int_{-D_\infty}^{\infty} y\overline{vP}\, dy. \tag{B.2}$$

In the limit (Fig. 2) of piecewise uniform P this integrated momentum flux becomes

$$\int_{-D_\infty}^{\infty} \overline{vu}\, dy = \iint_{\text{eddy}} dx\, dy\, yvP_e + \iint_{\text{shear}} dx\, dy\, yvP_1 \tag{B.3}$$

and the question is whether it is positive (directed toward low mean velocity), or negative ("counter gradient").

If the eddy is a point vortex with strength Γ (4.1) located at $y = y_0(t)$, then the first term on the right-hand side of (B.3) reduces to

$$\iint dx\, dy\, yvP_e = \Gamma y_0 \frac{dy_0}{dt}. \tag{B.4}$$

For a finite area eddy let $C_2(t)$ denote the closed material curve bounding the P_e fluid, and let $d\sigma$ denote a material area element ($dxdy$) inside C_2. Then

$$\iint dx\, dy\, yvP_e = P_e \iint d\sigma y \frac{dy}{dt} = \frac{P_e}{2}\frac{d}{dt}\iint d\sigma y^2 = \frac{P_e}{2}\frac{d}{dt}\iint dx\, dy\, y^2$$

$$= \frac{P_e}{6}\frac{d}{dt}\oint_{C_2} L_e^3(x, t)\, dx \tag{B.5}$$

where the contour integral is taken clockwise.

The last term in (B.3) may be evaluated in a similar way using the closed material

contour $C_1(t)$ = "abcd" in Figure 2a. This is composed of the entire interface ("ab"), a straight horizontal line ("cd") located in the undisturbed region $y = -D_\infty \to -\infty$, and two material branches ("bc," "da") constructed at $x = \pm\infty$ as follows. Initially ad and bc are chosen to be parallel, and they remain parallel at $t > 0$ as they are advected by the same $\overline{u}(y)$. Since $P_1 = 1$, the last term in (B.3) can be integrated in y to give

$$\int\int dy\, yvP_1 = \frac{1}{6}\frac{d}{dt}\oint_{C_1(t)} \eta^3(x, t)\, dx$$

where η is the ordinate of a point on C_1. The contribution of segment cd to the contour integral is constant in time and therefore does not contribute anything to the above equation. The contribution of segment bc is equal and opposite to the contribution of segment da and therefore their net contribution to the contour integral vanishes. Only the integral along ab does not vanish, and this gives

$$\int\int dx\, dy\, yvP_1 = \frac{1}{6}\frac{d}{dt}\int_{-\infty}^{+\infty} dx\, L_1^3. \tag{B.6}$$

Eq. (B.3) then becomes

$$\int_{-\infty}^{\infty} \overline{vu}\, dy = \frac{1}{6}\frac{d}{dt}\left[P_e \oint dx\, L_e^3 + \int_{-\infty}^{\infty} L_1^3\, dx\right] \equiv \frac{dM}{dt} \tag{B.7}$$

for a round eddy, and for a point vortex the average momentum flux is

$$\int_{-\infty}^{\infty} \overline{vu}\, dy = \frac{d}{dt}\left[\frac{\Gamma y_0^2(t)}{2} + \frac{1}{6}\int_{-\infty}^{\infty} L_1^3\, dx\right] \equiv \frac{dM}{dt}. \tag{B.8}$$

A similar procedure may be applied to the left hand side of the y-integral of (B.1) and since the right-hand side vanishes, we obtain

$$0 = \frac{d}{dt}\left[P_2 \oint dx\, L_e^2\, dx + \int_{-\infty}^{\infty} L_1^2\, dx\right] \equiv \frac{dQ}{dt} \tag{B.9}$$

for the round eddy, and for the point vortex

$$0 = \frac{d}{dt}\left[\Gamma y_0(t) + \frac{1}{2}\int_{-\infty}^{\infty} L_1^2\, dx\right] \equiv \frac{dQ}{dt}. \tag{B.10}$$

The quadratic-invariant Q in (B.9) is known from previous studies of barotropic shear layers [e.g. Stern (1989) p. 85; Dritschel (1988); Bell and Pratt (1993)], and was used here to check the numerics. It also implies that the speed at which the vortex moves toward the interface increases as the mean square interfacial disturbance increases.

REFERENCES

Bane, J. M., L. M. O'Keefe and D. R. Watts. 1989. Mesoscale eddies and submesoscale coherent vorticies: their existence near and interaction with the Gulf Stream. Proc. 20th International Colloquium on Ocean Hydrodynamics, Elsevier Oceanography Series, *50,* 501–518.

Bell, G. K. and L. J. Pratt. 1993. Eddy mean flow interaction theorems. Dyn. Atmos. Oceans, (submitted).

Bower, A. S. and T. Rossby. 1989. Evidence of cross-frontal exchange processes in the Gulf Stream based on an isopycnal RAFOS float data. J. Phys. Oceanogr., *21,* 173–180.

Dritschel, D. G. 1988. Nonlinear stability bounds for inviscid two dimensional flows. J. Fluid Mech., *191,* 575–581.

Halkin, D. and T. Rossby. 1985. The structure and transport of the Gulf Stream at 73W. J. Phys. Oceanogr., *15,* 1439–1452.

Hogg, N. G., R. S. Pickart, R. M. Haudry and W. J. Smethie. 1986. The northern recirculation gyre of the Gulf Stream. Deep-Sea Res., *33,* 1139–1165.

Knauss, T. A. 1969. A note on the transport of the Gulf Stream. Deep-Sea Res., *16* (Suppl.), 117–123.

Leaman, K. D., E. Johns and T. Rossby. 1989. The average distribution of volume transport and potential vorticity with temperature at three sections across the Gulf Stream. J. Phys. Oceanogr., *19,* 36–45.

Lee, T. N. and E. Waddell. 1983. On Gulf Stream variability and meanders over the Blake Plateau at 30N. J. Geophys. Res., *88,* C8, 4617–4631.

Meacham, S. P. 1991. Meander evolution on piecewise-uniform quasi-geostrophic jets. J. Phys. Oceanogr., *21,* 8, 1139–1170.

Melander, M. V., N. J. Zabusky and J. C. McWilliams. 1987. Asymmetric merger in two dimensions: which vortex is victorious. Phys. Fluids, *30,* 2610–2612.

Richardson, W. S., W. J. Schmitz Jr. and P. P. Niiler. 1969. The velocity structure of the Florida current from the Straits of Florida to Cape Fear. Deep-Sea Res., *16,* 225–231.

Smith, D. C. and G. P. Davis. 1989. A numerical study of eddy interaction with an oceanic jet. J. Phys. Oceanogr., *19,* 975–986.

Stern, M. E. 1985. Lateral wavebreaking and shingle formation in large scale shear flow. J. Phys. Oceanogr., *21,* 1622–1630.

—— 1991. Entrainment of an eddy at the edge of a jet. J. Fluid Mech., *228,* 343–360.

Stern, M. E. and G. R. Flierl. 1987. On the interaction of a vortex with a shear flow, J. Geophys. Res., *92,* C10, 10733–10744.

Received: *6 October, 1992;* revised: *11 May, 1993.*